Small Structures

small structures

www.small-structures.com

RESEARCH ARTICLE OPEN ACCESS

Passivating Contacts-Related Ultraviolet-Induced Degradation in Silicon Heterojunction Solar Cells

Binbin Xu[1,2] | Sara Alkhereibi[1,3,4] | Alexander Eberst[1,2] | Kai Zhang[1,2] | Rongda Zhang[1,5] | Joon-Ho Oh[6] | Astrid Besmehn[7] | Felix Gunkel[8] | Yuehui Li[9] | Tae Eun Hong[10] | Andreas Lambertz[1] | Karsten Bittkau[1] | Joachim Mayer[3] | Uwe Rau[1,2] | Kaining Ding[1]

[1]IMD-3 Photovoltaics, Forschungszentrum Jülich GmbH, Jülich, Germany | [2]Jülich-Aachen Research Alliance (JARA-Energy) and Faculty of Electrical Engineering and Information Technology, RWTH Aachen University, Aachen, Germany | [3]Ernst Ruska-Centre for Microscopy and Spectroscopy with Electrons, Forschungszentrum Jülich GmbH, Jülich, Germany | [4]Faculty of Mathematics, Computer Science and Natural Sciences, RWTH Aachen University, Aachen, Germany | [5]Faculty of Georesources and Materials Engineering, RWTH Aachen University, Aachen, Germany | [6]Ulsan Advanced Energy Technology R&D Center, Korea Institute of Energy Research, Ulsan, Republic of Korea | [7]IET-4 Elektrochemische Verfahrenstechnik, Forschungszentrum Jülich GmbH, Jülich, Germany | [8]PGI-7 Electronic Materials, Forschungszentrum Jülich GmbH, Jülich, Germany | [9]Institute of Quantum Materials and Physics, Henan Academy of Sciences, Zhengzhou, China | [10]Busan Center, Korea Basic Science Institute, Busan, Republic of Korea

Correspondence: Binbin Xu (b.xu@fz-juelich.de) | Alexander Eberst (a.eberst@fz-juelich.de) | Kaining Ding (k.ding@fz-juelich.de)

Received: 3 March 2026 | **Revised:** 28 April 2026 | **Accepted:** 21 May 2026

Keywords: 4D-STEM | nanocrystalline silicon carbide | transparent passivating contacts | ultraviolet-induced degradation

ABSTRACT

Hydrogen (H) is essential for the high performance of advanced crystalline silicon (c-Si) solar cells. Recently, H-related ultraviolet-induced degradation (UVID), which can compromise module stability, has attracted increasing attention from the photovoltaic (PV) industry, yet its underlying mechanisms remain incompletely understood. Here, the severity of UVID in silicon heterojunction (SHJ) solar cells is shown to depend strongly on the illuminated-side passivating-contact design, with transparent passivating contacts (TPCs) exhibiting markedly larger losses in open-circuit voltage (V_{OC}), short-circuit current (J_{SC}), and fill factor (FF) than conventional hydrogenated amorphous silicon (a-Si:H)-based SHJ contacts. Combined material characterizations and device analysis support a picture in which the high transparency of TPC shifts UV energy deposition toward the c-Si near-interface region, where UV-driven Si—H bond dissociation increases interfacial recombination and degrades chemical passivation. In parallel, UV exposure induces a pronounced resistivity increase in the hydrogenated nanocrystalline silicon carbide (nc-SiC:H) contact stack, consistent with local microstructural/electronic disorder and the possible involvement of enhanced sub-bandgap absorption, thereby raising series resistance (R_s) and limiting carrier collection. Collectively, these findings link contact optical transparency, H-related bond dynamics, and nc-SiC:H transport degradation to the distinct UVID signatures of SHJ architectures.

1 | Introduction

Crystalline silicon (c-Si) solar cells utilizing silicon heterojunction (SHJ) technology have seen a promising share in the continuously increasing global photovoltaic (PV) market. On the one hand, SHJ solar cells with front and back contact (FBC) structures and their modules are being produced on a gigawatt (GW) scale in PV factories and deployed in solar plants. The next generation of SHJ solar cells using back contact (BC) technology has been technically proven and has gradually entered the intensive process development phase [1]. Furthermore, extensive research on monolithic perovskite/silicon tandem solar cells has shown that SHJ solar cells are ideal candidates as the bottom cell for tandem technology [2]. Nevertheless, in the near future, the conventional

Binbin Xu and Sara Alkhereibi contributed equally to this study.

FBC structure will still dominate in mass-produced SHJ solar cells; therefore, the long-term performance and reliability are of primary concern to users who choose to install modules made of this type of SHJ solar cells.

In the last decade, efforts have been made to elucidate the stability failure mechanisms of SHJ solar cells and their modules. These investigations by different groups have shown that hydrogenated passivating contacts play an important role in failure. Failure occurs during the storage phase of the cell products before they are fabricated into solar modules. The dark degradation of SHJ solar cells is related to the reconstruction of the metastable intrinsic hydrogenated amorphous silicon (a-Si:H(i)) passivating layer [3]. More failures occurred after the deployment of the SHJ solar modules. According to a detailed review by Arriaga Arruti et al. in 2023, the failure modes of SHJ modules can be classified as degradation of encapsulation (such as discoloration, delamination), damp-heat (DH) -induced degradation caused by the heat-assisted water/moisture ingress, potential-induced degradation (PID), and ultraviolet-induced degradation (UVID) [4]. Degradation of hydrogenated materials in SHJ solar cells has been identified or suggested as a possible cause of the aforementioned failures. In a study on the effect of DH, Liu et al. attributed the loss of damp-heat stability of industrial-sized SHJ solar cells to the passivation degradation at the interface between a-Si:H and c-Si [5]. The cause was further identified as the oxidation of a-Si:H owing to moisture ingress. In the module that experienced PID failure, moisture led to a negative bias between the cells and the grounded frames. As a result, sodium ions (Na^+) diffused into the interface between indium tin oxide (ITO) and a-Si:H, which was identified as the source of degradation [6]. In 2022, Sinha et al. reported their systematic investigation on UVID in solar modules with different cell architectures [7]. Compared with the other modules, the SHJ solar module showed greater power loss after long-term UV exposure. They speculated that the damage originated from deterioration of the a-Si:H/c-Si interface. Later, there was an increasing interest in elucidating these mechanisms in detail. Ye et al. observed the UV-induced reduction of the total amount of bonded hydrogen in a-Si:H layers and the a-Si:H/c-Si interface by their Fourier transform infrared (FTIR) spectrum, which was regarded as the cause of UVID [8]. An investigation by Yang et al. continued in this direction; their studies on the carrier transport mechanism further associated UVID with a decrease in the H-related defect formation enthalpy (ΔH), both in the bulk a-Si:H layer and at the interface [9]. There has been a shift toward using hydrogenated microcrystalline/nanocrystalline materials instead of highly doped n-type amorphous silicon (a-Si:H(n)) for passivating contacts on the illuminated side, driven by the need to reduce parasitic absorption and contact resistivity (ρ_c). A recent study by Yang et al. argued that the phosphorus-doped hydrogenated microcrystalline silicon oxide (μc-SiO_X:H) layer becomes more porous and loses its hydrogen content after UV exposure, which is similar to the phenomenon observed in intrinsic amorphous silicon (a-Si:H(i)) layer [10]. In our recent work, we observed that applying a hydrogenated nanocrystalline silicon carbide (nc-SiC:H) transparent passivating contact (TPC) on the front side of SHJ solar cells led to a substantial UVID [11]. Despite these advances, most studies have focused exclusively on a single SHJ configuration, leaving the influence of front-side passivating contact selection on UVID not yet clarified.

Here, we show that the front contact architecture critically governs UVID in SHJ solar cells with an FBC structure. Compared with cells using an a-Si:H front stack, TPC-based devices suffer much larger efficiency losses under UV exposure. Integrated performance, optical–electrical, and material analyses reveal that passivation deterioration and output current loss originate from the UV-induced Si—H bond rupture and microstructural rearrangements. Together, these findings highlight the crucial role of front-side passivating contact design in determining UV stability.

1.1 | UV Test Setup

Unlike studies on DH-induced degradation and PID, there is still no uniform standard for UVID investigation. Table 1 summarizes the UV irradiation and test conditions reported in the literature for UVID investigations performed on bare cells. In most studies, ultraviolet A (UVA, 320–400 nm) lamps were selected as the light source to mimic UV irradiation from the sun, considering the small portion of ultraviolet B (UVB, 280–320 nm) in the typical AM1.5G spectrum. However, the lamp and the spectral intensity varied between the investigations. Some lamps have irradiance centered at 340 nm, while others emit a spectrum centered at 365 nm. The settings of the spectral intensities were varied. In addition, there is no standard for ending irradiance. In ref. [7], UV irradiation continued for 2000 h, while irradiation was stopped at 48 h in ref. [9]. Other studies chose the total UV dose, which is the product of the UV intensity and irradiation duration, as the indicator of ending experiments. Compared with the method calculated in hours, the total UV dose is easier to quantify and compare between the experiments. Moreover, the UV dose is recommended in established standards related to UV, such as IEC 61215.

The UV irradiation experiments in this study were conducted in a UV irradiation chamber supplied by Opsytec Dr. Groebel GmbH, Germany, equipped with UVA 352 nm lamps manufactured by Sankyo Denki Co., Ltd. Figure 1 presents the spectrum of the UVA lamp measured using a monochromatic detector along with the AM1.5G solar spectrum in the UV-related range. The total UV irradiance, defined by integrating the spectrum up to 400 nm, was measured to be 56 W m^{-2}. Within this range, the irradiance up to the 365 nm cutoff was 22 W m^{-2}. The cutoff value is recommended in Ref. [12], as the authors suggested, UV photons with wavelengths above 365 nm may not possess sufficient energy to effectively break Si—H bonds. The accumulated UV dose was automatically detected and counted by using an integrated component in the irradiation chamber. Based on existing literature, the total UV dose for a complete exposure cycle of solar cells was set to 60 kWh m^{-2}. According to Yang et al., UVID may be a temperature-dependent process [9]. All experiments in this study were conducted at room temperature to focus on the degradation induced solely by UV irradiation. The temperature in the UV irradiation chamber was monitored using type K Class 1 thermocouples. As shown in Figure S1, the chamber temperature remained stable during the entire irradiation process, confirming that any UV-induced thermal effects were negligible. Sinha et al. calculated the acceleration factor of their setup by dividing the UVA intensity at 340 nm by that of the AM1.5G spectrum [7]. However, this method is wavelength specific and applies only to a particular lamp setup. Instead, this

TABLE 1 | UVID test setup and conditions for unencapsulated cells reported in the literature and employed in this study.

Source	UV lamps	Criteria for ending irradiance	Testing temperature, °C	Accelerating factor (ratio between intensities)
Sinha et al. [7]	UVA-340 nm fluorescent lamps ($1.24\,W\,m^{-2}\,nm^{-1}$ @ 340 nm)	Up to 2000 h	45°C ± 2°C	UVA/AM1.5G@340 nm
Ye et al. [8]	UVA with irradiance centered at 365 nm ($200\,W\,m^{-2}$)	UV dose equivalent to $60\,kWh\,m^{-2}$	40°C	—
Yang et al. [10]	UVB + UVA (280–400 nm, $200\,W\,m^{-2}$)	UV dose = $20\,kWh\,m^{-2}$	60°C	—
Yang et al. [9]	UVA with irradiance centered at 365 nm ($50\,W\,m^{-2}$)	Up to 48 h	27°C/100°C	—
Thome et al. [12]	UVA-340 nm lamps ($226\,W\,m^{-2}$)	UV dose = $60\,kWh\,m^{-2}$	60°C	UVA/AM1.5G, range dependent
This work	UVA-352 nm lamps ($56\,W\,m^{-2}$)	UV dose = $60\,kWh\,m^{-2}$	$25^{+0.3}_{-0.4}$°C	UVA/AM1.5G 1.0 (280–365 nm); 1.2 (280–400 nm)

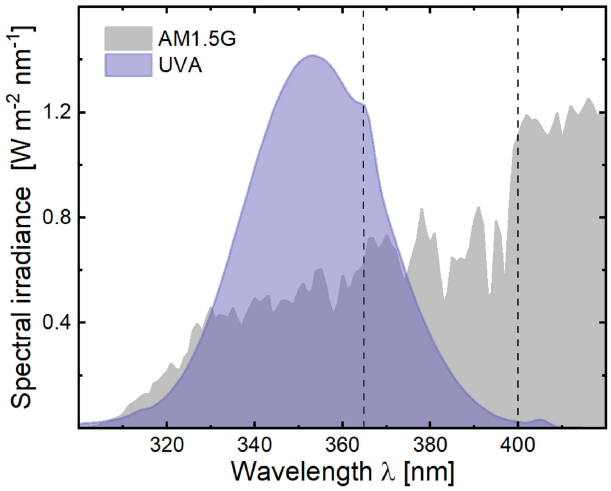

FIGURE 1 | The UVA spectrum used in this study and the AM1.5G spectrum.

study adopted a more universal approach, as reported by Thome et al., which calculates the ratio of the spectrum over a defined wavelength range [12]. Using the same approach as in Ref. [12], the acceleration factors were determined to be 1.0 and 1.2 for the upper integration limits of 365 and 400 nm, respectively.

2 | Results and Discussion

Widespread reports on UVID highlight the importance of considering the impact of UV exposure when designing and optimizing the structure of SHJ solar cells. The calculated absorption profile of silicon solar cells versus the depth into the absorber indicates that the absorption of the ultraviolet spectrum occurs only a few micrometers from the surface [13]. In theory, the illuminated-side architecture is the primary contributor to UVID in the SHJ solar cells. To verify this, we evaluated the effect of UV irradiation on cells incorporating two front-side passivating contacts. One is the standard contact consisting of n-type phosphorous-doped a-Si:H and intrinsic a-Si:H (a-Si:H(*n*)/a-Si:H(*i*)) in conventional SHJ solar cells, referred to as SHJ contacts in this work. The other type of contact is a TPC based on nc-SiC:H, which represents a proof-of-concept design proposed in an earlier work [14]. Unlike the SHJ contact, to obtain an optimal passivation quality, a wet-chemically prepared silicon tunnel oxide (SiO_X) layer must be prepared before the hot-wire chemical vapor deposition (HWCVD) of nc-SiC:H. The nc-SiC:H was designed as a double layer to balance the trade-off between passivation and conductivity, as detailed in our previous work [14]. The schemes of the cell structures with SHJ or TPC contacts are shown in Figure 2h. The same rear junction configuration composed of intrinsic a-Si:H and p-type boron-doped a-Si:H (a-Si:H(*i*)/a-Si:H(*p*)) was adopted to minimize the influence of the rear side. Figure 2 presents the changes in cell performance induced by UV irradiation. The accumulated UV dose was maintained at $60\,kWh\,m^{-2}$. As shown in Figure 2a, UV exposure reduces the efficiency of both types of samples, with an average loss of $2.58\%_{abs}$ for SHJ and a much larger $9.34\%_{abs}$ for TPC. To the best of our knowledge, such a severe extent of UVID has not been documented for heterojunction solar cells with other front-side architectures [7–10, 12]. Figure 2b shows a pronounced short-circuit current density (J_{SC}) loss of approximately $4.66\,mA\,cm^{-2}$ in TPC samples after UV irradiation, whereas SHJ samples lost only approximately $1.19\,mA\,cm^{-2}$, which is still larger than the minor changes reported by others [7, 8]. UV-induced reduction in open-circuit voltage (V_{OC}) has been widely reported. For instance, Sinha et al. observed a decrease in V_{OC} of $3\%_{rel}$ after UV exposure for 2000 h on front-junction SHJ solar cells [7], where the emitter contact was directly illuminated. Together with two additional studies on similar architectures [9, 12], these results may not fully represent UVID behavior under more practical conditions, since the rear-junction configuration is predominantly used in industry.

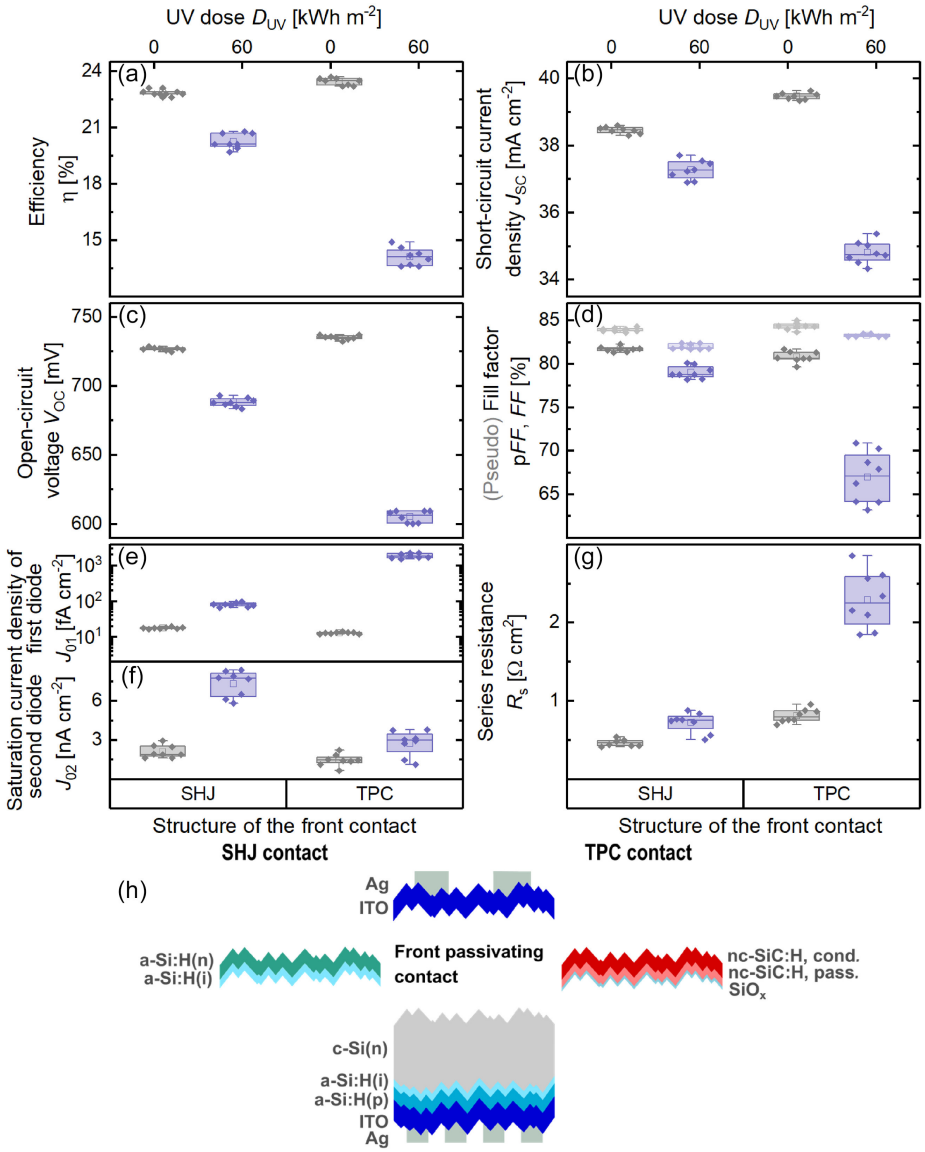

FIGURE 2 | Evolution of (a) efficiency, (b) short-circuit current density, (c) open-circuit voltage, (d) pseudo fill factor and fill factor, saturation current density of (e) first diode and (f) second diode, and (g) series resistance of silicon heterojunction solar cells using (h) a-Si:H based SHJ contact or nc-SiC:H based TPC contact after UV irradiation with a UV dose of 60 kWh m^{-2}. In this scheme, nc-SiC:H, pass. and nc-SiC:H, cond. represent the passivation layer and the conductive layer in the double-layer structure of nc-SiC:H, respectively.

In fact, several works have examined the UVID in rear-junction SHJ cells. A 1%$_{rel}$ loss of V_{OC} in the rear-junction SHJ solar cells was observed after exposure to 60 kWh m^{-2} at 40°C [8]. In this study, substantial V_{OC} losses are also observed, with reductions of approximately 38.7 mV for SHJ samples and 129.8 mV for TPC samples, as shown in Figure 2c. The relative V_{OC} loss of SHJ samples is 5.3%$_{rel}$, exceeding the value reported in ref. [8]. This difference may stem from the UV testing temperature, since our experiments were conducted at room temperature, whereas theirs were performed at 40°C. Elevated temperatures may cure some of the damage caused by UV irradiation. This observation supports the view that UVID is temperature-dependent [9]; however, the opposite trend observed here indicates that a systematic study is still lacking. On the other hand, the more pronounced V_{OC} loss in the SHJ samples may be due to the thinner front contact, allowing more UV photons to reach the a-Si:H/c-Si interface, thus weakening chemical passivation.

The much greater reduction in V_{OC} on TPC samples was rarely reported. To further identify the reason, we simply describe V_{OC} as follows:

$$V_{OC} = \frac{kT}{q} \ln\left(\frac{J_{ph}}{J_{01} + J_{02}} + 1\right) \quad (1)$$

where k is the Boltzmann constant, T is the temperature in Kelvin (K), q is the elementary charge, J_{ph} is the photogenerated current density, and J_{01} and J_{02} are the saturation current densities of the first and second diodes, respectively, obtained by modeling the solar cells with a two-diode equivalent circuit.

The evolutions of J_{01} and J_{02} are shown in Figure 2e,f, respectively. After UV exposure, J_{01} increases by about 63.2 fA cm^{-2} for SHJ samples and 1885.2 fA cm^{-2} for TPC samples, while J_{02} shows

an increase of approximately 5.2 and 1.3 nA cm^{-2}, respectively. The much stronger increase in J_{01} accounts for the significant disparity in V_{OC} loss between SHJ and TPC samples, indicating enhanced recombination in the quasi-neutral bulk and at the surface. In addition, since the rear structure is identical, the remaining discrepancy in V_{OC} reduction can be attributed to defect generation in the distinct front contacts.

Figure 2d shows the changes in the pseudo fill factor (pFF) and fill factor (FF), and Figure 2g shows the change in series resistance (R_s). A sharp FF loss of 13.9%$_{abs}$ is observed for the TPC samples. In contrast, the FF of the SHJ samples reduces by 2.7%$_{abs}$, mainly due to a 1.9%$_{abs}$ reduction in pFF. Note that the FF behavior of SHJ samples under UV irradiation can vary with their initial values, which is shown in Figure S2 and discussed in the Supporting Information. The FF loss behavior of the TPC samples is well defined and obviously dominated by R_s. After UV exposure, R_s increases by approximately 1.5 Ω cm^2, while the decline in pFF (1.0%$_{abs}$) accounts for only a small fraction of the total loss. To further investigate, the contact resistivities (ρ_c) of the TPC samples were measured with special patterns prepared on the same substrate using the transfer length method (TLM) before and after UV irradiation. Figure S3 shows the changes in ρ_c between Ag and ITO on the front and rear sides of the samples, as well as for the entire Ag/ITO/TPC/c-Si stack. While the Ag/ITO contacts exhibited almost no variation, the stack ρ_c increases by 358.5 mΩ cm^2, indicating that UV irradiation does not affect the metal/ITO interface. Instead, degradation and a rise in resistivity take place in the underlying region, involving both interfacial and bulk components.

The pronounced V_{OC} and FF losses of the TPC samples suggest significant UV-induced modifications in the material properties and microstructure of the TPC contacts. To further study the front-contact–dominated V_{OC} loss, symmetric lifetime samples with identical contacts (SHJ (a-Si:H(n)/a-Si:H(i)) or TPC) on both sides of the c-Si wafer were subjected to UVID experiments. These samples were irradiated together with the solar cells to monitor the degradation of passivation quality. Figure 3a,b shows the effective lifetime(τ_{eff}) as a function of excess carrier density (Δn) for the SHJ and TPC samples, respectively. The two samples have nearly identical initial lifetimes, reflecting similar passivation quality, but their UV stability differs markedly. For the TPC-passivated samples, even a UV dose of 15 kWh m^{-2} results in a pronounced decrease in τ_{eff} across all carrier injection levels (i.e., Δn). A hump appears in the τ_{eff} –Δn curve at ~1×10^{15} cm^{-3}, indicating severe degradation of chemical passivation [15] and revealing weak field-effect passivation from the highly doped n-type nc-SiC:H layer. Prolonged UV irradiation further reduces the chemical passivation, and the resulting recombination ultimately overwhelms the weak field-effect contribution. In contrast, the SHJ-passivated samples show a much smaller decrease in τ_{eff} with progressive UV exposure, reflecting significantly less chemical passivation loss compared with the TPC samples under identical conditions. The photoluminescence (PL) lifetime images in Figure S4 provide spatially resolved evidence for the observed passivation loss and lifetime reduction. Figure 3c,d presents the external quantum efficiency (EQE) and 1–reflectance (1–R) spectra before and after UV exposure, from which distinct degradation behaviors can be identified for SHJ and TPC cells. The reflectance of the samples remains almost unchanged. With extended UV exposure, the spectral response below $\lambda\sim1000$ nm progressively decreases. According to our previous simulations on rear junction cells [13], this evolution of the EQE curve can be ascribed to an increased surface recombination velocity at the front surface (S_{front}). After UV exposure to 60 kWh m^{-2}, a hump emerges in the EQE spectrum of the TPC cell around $\lambda=1000$ nm. This feature resembles the simulated curve with S_{front} of 200 cm s^{-1} in ref. [13], evidencing severe front surface recombination.

Both the lifetime measurements and the spectral response show that the UV-induced increase in front-surface recombination depends on the front-side contact configuration. This interpretation is further supported by a directional-illumination experiment on TPC solar cells in Figure S5, in which front-side UV illumination causes markedly stronger degradation than back-side illumination. Intuitively, the optical design of the front-contact stack is a natural first candidate to explain the observed difference. The absorbed UV-related photon flux (300–420 nm) and the corresponding energy loss in each layer are calculated and plotted as percentages in Figure 3e,f. The incident UV photon flux was calculated from the UV spectrum shown in Figure 1. Based on the measured reflectance spectra of cells with SHJ or TPC contacts, the UV photon fluxes absorbed in each cell type were obtained by multiplying the incident UV photon flux by the wavelength-dependent absorptance (A, with $A=1–R$). Since the reflectance spectrum was measured directly on the cells using a 1.5 cm × 1.5 cm light spot, the effect of the front-side fingers is inherently included, thus the resulting absorptance represents the actual absorption in the solar cells. In state-of-the-art heterojunction solar cells, the passivating-contact/c-Si interface is the key region controlling chemical passivation and surface recombination. Here, the interface should be understood in the sense of device-physics as a near-interface region that extends a few nanometers into both the contact stack and the c-Si, in which the generation and saturation of dangling bonds govern the chemical passivation quality [16]. In this work, the near-interface regions are denoted as the interfacial affected zone (IAZ). The layer thicknesses used in the optical calculations are listed in Table S1. Owing to the ultrathin thickness and wide bandgap of the SiO_X tunneling layer [17], it is not taken into consideration for the optical calculation. The IAZ thicknesses are estimated from the thickness-dependent implied open-circuit voltage(iV_{OC}) of the corresponding cell precursors, as shown in Figure S6. Based on the actual device stack, the full a-Si:H(i) layer (3.5 nm) and the nc-SiC:H passivation layer (5.2 nm) are assigned to the IAZs. For both devices, the IAZ thickness on the c-Si side is assumed to be 3.5 nm. The absorption coefficient of each layer used for the calculation is plotted in Figure S7.

As shown in Figure 3e, the highly transparent concept [14] of TPC enables a larger fraction of UV photons to be absorbed on the c-Si side, within the IAZ and further into the wafer bulk, whereas the SHJ structure exhibits substantial parasitic absorption in the a-Si:H stack. Owing to their high photon energy, UV photons generate carriers with excess energy above the band edges. Under open-circuit UV-irradiation conditions, these carriers relax predominantly via thermalization and subsequently recombine. To quantify thermalization loss, we integrate energy loss, i.e. UV photon energy minus bandgap energy, over the UV-relevant spectral range and evaluate its layer wise shares in Figure 3f. For TPC, approximately 98% of the thermalization loss occurs in c-Si,

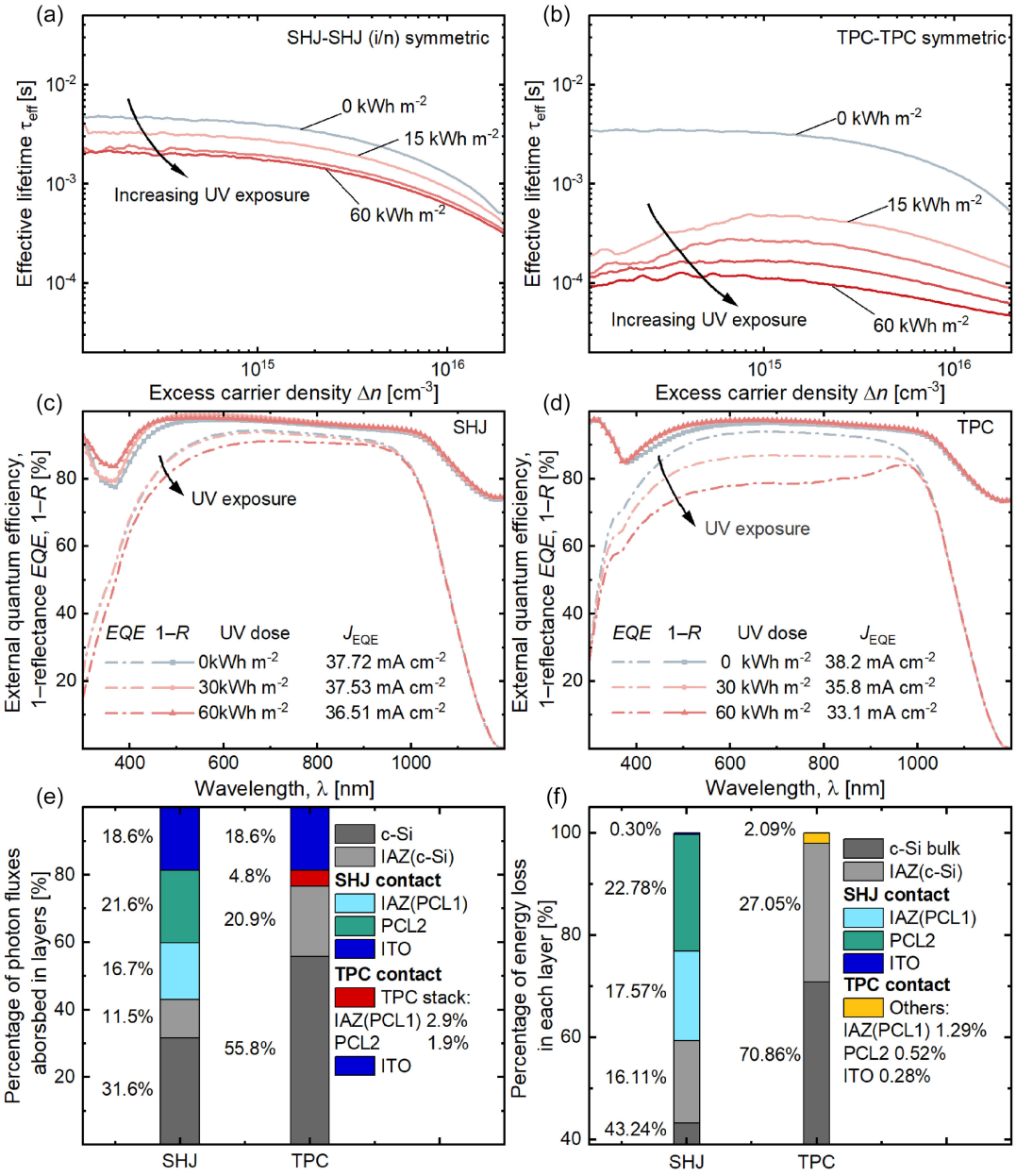

FIGURE 3 | Effective carrier lifetime as a function of excess carrier density for symmetrical samples with (a) SHJ contacts and (b) TPC contacts on both sides. The solid lines with arrows indicate the evolution of lifetime curves with increasing UV exposure. External quantum efficiency and 1–reflectance spectra of heterojunction cells with (c) SHJ front contact and (d) TPC front contact measured before and after UV exposure at doses of 30 and 60 kWh m^{-2}, respectively. (e) Percentage of photon flux absorbed and (f) percentage of energy loss in specific layers of the SHJ and TPC solar cells. "PCL1" and "PCL2" refer to the passivating contact layers, numbered from the substrate side toward the ITO. "IAZ" refers to the interfacial affected zone.

of which, 27% is dissipated within the IAZ on the c-Si side. While for the case of SHJ, about 59% occurs in c-Si, including 16% in the c-Si side IAZ, while 41% is deposited in the a-Si:H stack, including 18% in the a-Si:H side IAZ.

This difference in thermalization partitioning implies that thermalization, particularly when concentrated in the c-Si-side near-interface region, could be a driving mechanism for the distinct UV-induced passivation degradation in TPC and SHJ. In c-Si, thermalization energy is converted into lattice vibrations and dissipated as heat. However, given the long mean free path of phonons in c-Si [18] and the continuous irradiation conditions, a non-negligible fraction of this energy can be transported toward the near-interface region. While the energy released in a single relaxation event is below the Si—H bond energy, of approximately 2.75 eV [19], a sustained, high phonon population may increase the likelihood of localized multi-phonon activation of Si—H bond rupture at the c-Si surface. Crucially, rupture of c-Si surface Si—H bonds directly creates unsaturated dangling bonds at the interface, thereby removing the very species responsible for chemical passivation. This pathway is expected to most strongly increase the effective surface recombination velocity and, consequently, reduce V_{OC}. From the perspective of SHJ, despite the considerable thermalization loss deposited in the a-Si:H stack and the associated phonon-like energy dissipation [20], the released energy is expected

to primarily promote the formation of dangling bonds in the a-Si:H bulk, which supports the observations in the literature [8, 10]. These bulk defects generated in the near-interface region can act as recombination centers, however, their impact on V_{OC} is expected to be weaker than that of unsaturated dangling bonds created directly at the c-Si surface. This interpretation is consistent with our observations: If thermalization-driven defect creation in the a-Si:H stack was comparably effective in reducing V_{OC}, a stronger V_{OC} loss would be expected for SHJ than for TPC at comparable UV dose, which is not observed.

Beyond the thermalization process, subsequent recombination can further amplify UV-induced passivation degradation by releasing energy locally and facilitating additional bond rupture. For high-quality wafers, Auger recombination within the c-Si side IAZ could generate secondary phonons via electron–phonon scattering [21], but this contribution is expected to be smaller than the primary thermalization term. In SHJ, SRH recombination in the comparatively defect-rich a-Si:H can be a more efficient driver of localized multi-phonon excitation than thermalization alone, consistent with established microscopic pictures of the Stabler–Wronski process [22, 23]. Nevertheless, this pathway predominantly reinforces bulk defect creation and propagation in a-Si:H and is therefore expected to impact carrier transport more than an interface-limited V_{OC} loss. Another possible contribution is the repeated charging and discharging [24, 25] of pre-existing interfacial dangling bonds, as well as dangling bonds created during UV exposure. Such charge-state cycling can locally release energy and may facilitate nearby bond rupture through a localized multiphonon activation pathway. However, this mechanism alone is unlikely to account for the markedly stronger UV-induced passivation loss observed for TPC. Although the chemically grown SiO_X/c-Si interface via Piranha treatment can exhibit a higher as-prepared interface-state density (D_{it}), of approximately 1.3×10^{12} cm^{-2}, than an optimized a-Si:H(i)/c-Si interface [26, 27], the subsequent deposition of nc-SiC:H in the HWCVD chamber is expected to further reduce the effective D_{it} via hydrogen passivation under H-rich conditions. This is consistent with the comparable initial passivation quality of TPC and SHJ prior to UV exposure. Therefore, differences in the initial density of interfacial dangling bonds are unlikely to provide a stronger "starting condition" that could by itself explain the much more pronounced UV-induced passivation loss in TPC. Moreover, the microscopic energy dissipation associated with charging and discharging of interfacial dangling bonds should be fundamentally similar at SiO_X/c-Si and a-Si:H(i)/c-Si interfaces, making a specific acceleration of a localized multiphonon bond-rupture pathway at the SiO_X/c-Si interface less likely. In addition, energy release due to recombination and charge-state-cycling is not intrinsically UV-exclusive and should also occur under visible illumination. If these processes dominated the observed passivation degradation, a comparable passivation loss would be expected under visible light, which seems implausible.

Based on the discussion above, a plausible driving mechanism for UV-induced passivation loss is thermalization in the c-Si-side near-interfacial region. The stronger degradation observed for TPC is consistent with its dominant UV absorption and energy deposition in this region. Notably, the simplified model does not account for sub-bandgap UV absorption via band-tail and defect states within the TPC contact stack, which may be more relevant to the pronounced, R_s-limited fill-factor loss. Given the intrinsic nature of SiC and its nanocrystalline phase, band-tail and defect states can extend deep into the gap, in some cases approaching mid-gap energies [28]. Excitation into these localized states promotes highly localized multiphonon relaxation, concentrating the released energy in the immediate bonding environment and thereby facilitating Si—H bond rupture without requiring strong overall UV absorption in the nc-SiC:H stack. Substantiating this hypothesis requires direct evidence of UV-induced changes in the TPC-contact materials. In addition, detailed measurements of hydrogen behavior and potential microstructural evolution are needed to further elucidate the severe UVID observed in TPC solar cells. The following discussion addresses these aspects.

The evolution of ITO optical and electrical properties could, in principle, contribute to UVID. Figure 4a–c compare the transmittance (T), reflectance (R), and resistivity (ρ) of ITO before and after UV exposure. After irradiation to 60 kWh m^{-2}, no discernible change in T or R is observed on the ITO/Corning glass samples. Hall measurements on the same samples reveal only a negligible change in ρ (Figure 4c), indicating that ITO contribution to the observed R_s increase is minimal. These results are independent of the UV absorption in ITO (proportional to the thickness), confirming that the ITO layer remains largely stable under UV irradiation. Figure 4d presents the evolution of T and R for the double-layer nc-SiC:H stack owing to UV exposure. While T remains unchanged, R decreases compared to the initial state. To quantify the absorption change, the external reflection corrected absorption coefficient (α_{corr}) is calculated as

$$\alpha_{corr} = -\frac{1}{d}\ln\frac{T}{(1-R)} \tag{2}$$

where d is the film thickness obtained by fitting the spectroscopic ellipsometry data. Here, the nc-SiC:H stack thickness is approximately 23 nm, similar to the case of TPC contacts used in the cells.

The α_{corr} versus photon energy (E_{photon}) curves for the nc-SiC:H stack are displayed in Figure 4e. An obvious shift of the curve toward lower energy is observed after UV exposure, with the optical bandgap (E_{04}) decreasing from 3.07 to 2.89 eV. The UV-induced red shift of the absorption edge is consistent with increased contributions from band-tail states or defect-related states in the nc-SiC:H stack. Together with previous reports of pronounced low-energy free-carrier absorption in nc-SiC:H [14], this suggests the possibility of enhanced sub-gap absorption. However, the present UV–vis-based data does not reliably resolve the very low-intensity absorption region, so no quantitative conclusion is drawn here. In the device stack, this optical change is expected to be largely screened by ITO. Accordingly, no variation is detected for the ITO/nc-SiC:H stack in Figure S8 within experimental sensitivity. Therefore, when combined with the previously observed J_{SC} loss or EQE reduction in solar cells, this optical result suggests that the degradation is more likely dominated by enhanced recombination at the TPC/c-Si interface rather than the increased bulk absorption in nc-SiC:H. The most pronounced UV-induced change is observed in the electrical properties of nc-SiC:H. As shown in Figure 4f, its ρ increases from 15.1 to 109.2 Ω cm with increasing UV dose, consistent with the R_s increase of TPC cells. A sharp rise occurs

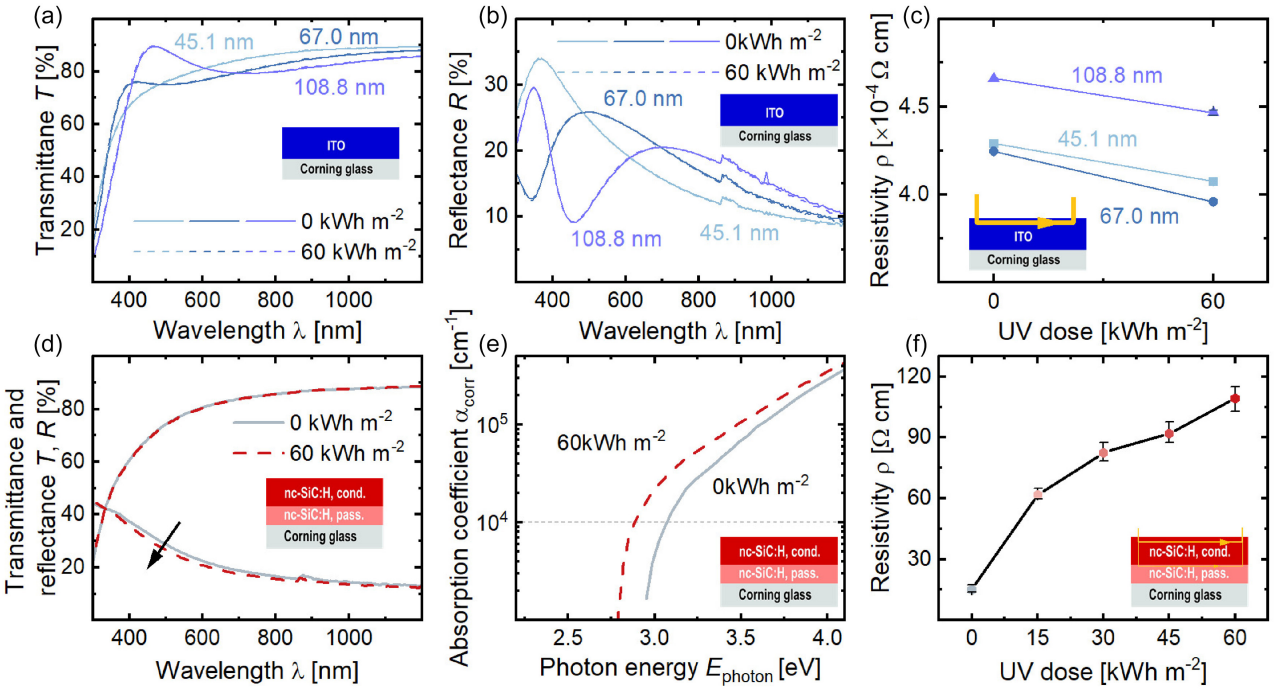

FIGURE 4 | (a) Transmittance, (b) reflectance, and (c) resistivity of ITO layers with different thicknesses before and after 60 kWh m^{-2} UV exposure. (d) Transmittance/reflectance and (e) absorption coefficients of a double-layer nc-SiC:H stack before and after 60 kWh m^{-2} UV exposure. The solid arrows serve as visual guides, and the dotted line indicates an absorption coefficient of 10^4 cm^{-1}. (f) Resistivity of double-layer nc-SiC:H stack as a function of UV exposure.

after the first 15 kWh m^{-2}, followed by a slower slope, suggesting that the UV-induced resistivity change in nc-SiC:H becomes less pronounced with extended irradiation.

To probe bonding configurations, FTIR spectra were acquired on samples without ITO to avoid screening effects [29]. To emulate the device stack, a full TPC contact was deposited on oxidized c-Si. In addition, single-layer nc-SiC:H films were deposited on polished c-Si to separately represent the passivation and conductive layers. As shown in Figure S9, UV exposure does not induce a measurable change in the absorption intensity of FTIR Si−C stretching mode (I_{Si-C}) of nc-SiC:H. By contrast, the Si−H stretching mode exhibits a clear UV-induced evolution in both intensity and peak position. Figure 5a shows distinct initial Si−H peak positions for the two nc-SiC:H layers, reflecting distinct local bonding environments [30]. The Si−H peak is centered at 2100 cm^{-1} for the passivation layer and shifts to 2133 cm^{-1} for the conductive layer. The latter approaches the 2145 cm^{-1} component commonly assigned to Si−H on Si sites with C backbonds in a-SiC:H [31, 32], indicating a denser, more SiC-like local environment. In contrast, the position of 2100 cm^{-1} is widely attributed to void-/grain-boundary–related Si−H configurations [30, 31]. Consistently, the higher absorption intensity of the Si−H stretching mode (I_{Si-H}) of the passivation layer suggests more Si−H sites hosted by a nanocrystal–amorphous mixed structure with abundant grain boundaries, while the conductive layer is more compact with larger grains and fewer boundaries. This contrast can be rationalized by the lower filament temperature and higher deposition rate used for the passivation layer, which favor rapid nucleation and smaller grains [14, 33]. Upon UV irradiation, I_{Si-H} decreases markedly for all samples, indicating Si−H bond dissociation across the double-layer stack and the interface between TPC contact and c-Si, which supports above assumption regarding sub-bandgap UV absorption. Moreover, the Si−H peak of the conductive layer shifts toward lower wavenumbers (2125 cm^{-1}), suggesting a reconfiguration of the remaining Si−H bonding environment.

Understanding the hydrogen behavior after Si−H bond rupture within the TPC contact is important for clarifying the UVID mechanism. Therefore, secondary ion mass spectrometry (SIMS) was performed to gain insight into hydrogen redistribution. Figure 5b shows the time-of-flight secondary ion mass spectrometry (ToF-SIMS) depth profiles of H, O, Si, and C for the TPC contact deposited on polished c-Si wafers. To minimize sample-to-sample variability, the profiling was performed on the same sample before and after UV irradiation at a UV dose of 30 kWh m^{-2}. As SIMS is destructive, the profiles were acquired at different lateral positions and can show offsets due to small thickness variations. Therefore, they are realigned to the c-Si surface for comparison. A similar profile measured on SHJ sample is shown in Figure S10. Unlike the pronounced H diffusion reported under UVID in the contact stack and even into the Si bulk [7], which is often considered a characteristic signature of UV-induced degradation, the present ToF-SIMS profiles show no such diffusion-like behavior. An interfacial gradient is already present in the as-prepared state, reflecting the intrinsic interfacial transition and the finite depth resolution of sputter profiling. Importantly, UV exposure does not induce additional broadening or a measurable change in the interfacial slope at either the ITO/contact or contact/c-Si interface. Thus, no diffusion-like signature, typically manifested in SIMS depth profiling as interfacial broadening and/or a change in profile slope relative to the pristine state [34], is detected within the sensitivity of the current ToF-SIMS depth profiles. Furthermore, an independent

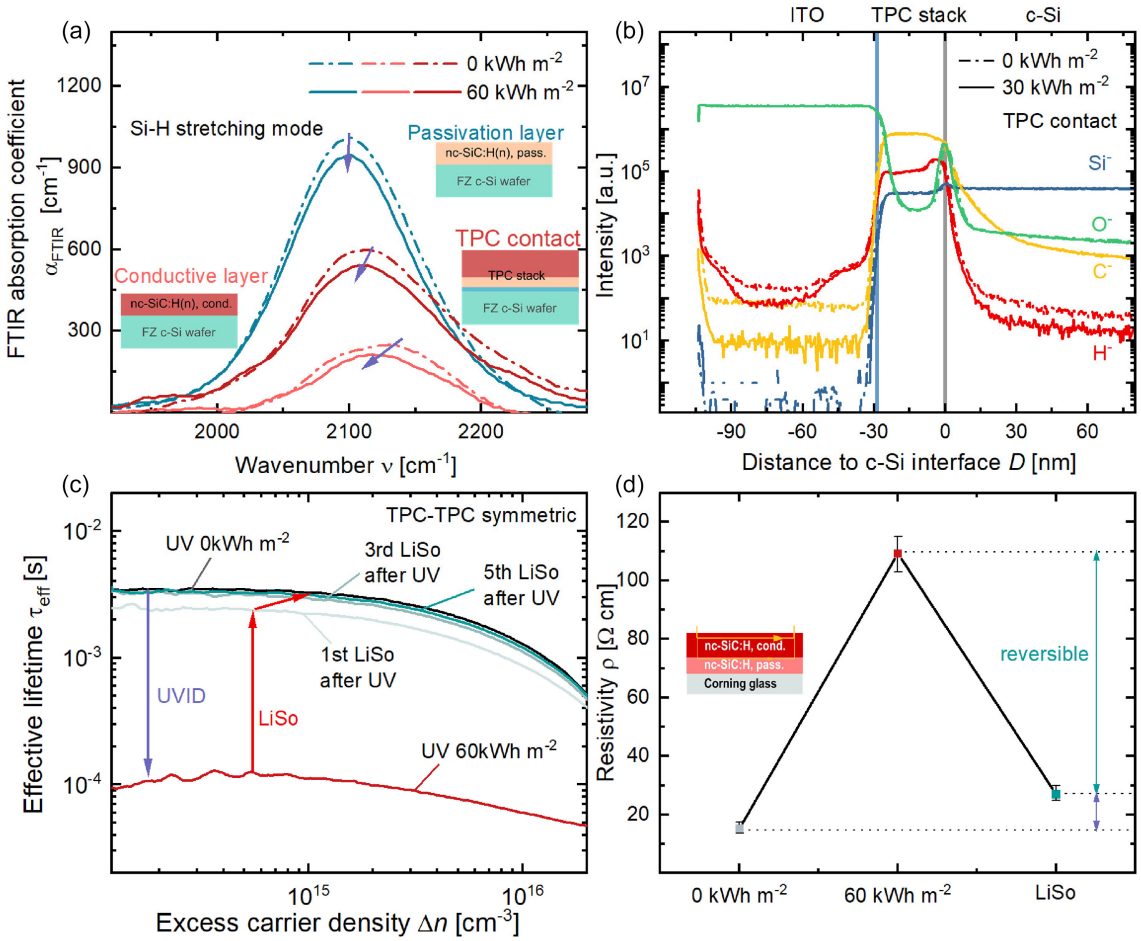

FIGURE 5 | (a) FTIR spectra showing the evolution of the Si—H stretching absorption peaks in nc-SiC:H due to UV irradiation. (b) ToF-SIMS depth profiles of the sample with a TPC contact, measured before and after UV irradiation to a dose of 30 kWh m^{-2}. The gray line represents the c-Si surface used for profile realignment, and the blue line represents the ITO/nc-SiC:H interface. (c,d) Evolution during UV exposure and subsequent heat-assisted light soaking (LiSo): (c) carrier injection–dependent effective carrier lifetime of TPC–TPC symmetric samples and (d) resistivity of the double-layer nc-SiC:H stack. Solid arrows in the panels are guide to the eye.

SIMS setup provides quantified H concentration depth profiles of the TPC contact in Figure S11. Consistently, comparing the pre- and post-UV profiles reveals no diffusion-like signature. Given the finite depth resolution, these results rule out pronounced, long-range hydrogen redistribution across the interfaces, but cannot exclude highly localized rearrangement confined within the few-nanometer-thick region like IAZ.

Interestingly, the subsequent heat-assisted light soaking (LiSo) treatment on UV-irradiated TPC samples provides further insight into the behavior of hydrogen under UV and its relationship to the passivation. Figure 5c shows stepwise lifetime measurements on TPC–TPC symmetric samples. LiSo applied after UV exposure induces a stepwise recovery. The first cycle restores the lifetime substantially, whereas subsequent cycles yield smaller, incremental improvements. After the fifth cycle, the curves approach a nearly stable level close to the pristine state, indicating that a large fraction of the UV-induced passivation loss is reversible under LiSo. Combined with the SIMS profiles, this behavior suggests that UV-related energy deposition at the c-Si interface is sufficient to break Si—H bonds but insufficient to drive long-range hydrogen redistribution across the interfaces. Instead, the released H species likely remain near the c-Si interface and close to their original bonding sites. Once additional energy is supplied during LiSo, rebonding can proceed. Recovery of Si—H bonding in the TPC contact after LiSo is supported by the FTIR spectra in Figure S12. Observations for SHJ samples, both in literature [8] and in Figure S13, are consistent with this hypothesis. Notably, the recovery kinetics differ between SHJ and TPC. A single LiSo treatment is sufficient for SHJ, whereas multiple LiSo cycles are required for TPC to gradually, but not fully, recover the passivation loss, as further evidenced by device-level evolution in Figure S14b. This difference points to distinct bonding environments associated with the different contact materials. Moreover, the recovery observed here requires illumination at tens of suns and temperatures above 150°C [35]. Under field conditions (~1 sun and module temperatures of ~60°C), only limited self-recovery is expected, unlikely to approach the extent achieved here. This is consistent with our previous UVID observations at 60°C [11].

In parallel, the effectiveness of LiSo in mitigating the UV-induced resistivity increase of the nc-SiC:H stack provides further insight into the origin of the UV-driven R_s increase. Notably, a residual component remains unrecovered under the present LiSo protocol, as shown in Figure S14d. In our previous

work, a LiSo-induced R_s reduction was observed for both SHJ and TPC devices and was discussed in the context of band-tail states, resistivity and the thermal contribution of LiSo [35, 36]. Consistently, Figure 5d shows that LiSo recovers most of the UV-induced increase in ρ, yet a residual of 11.9 Ω cm above the pre-UV value. Taken together with Figure 4f and the discussion above on sub-bandgap UV absorption, these results motivate the following hypothesis for the evolution of ρ. Sub-bandgap UV absorption in nc-SiC:H may promote Si—H bond dissociation within the nc-SiC:H network, consistent with the FTIR observations. Such bond dissociation can be accompanied by local structural rearrangements that increase electronic disorder, for example, by enhancing band-tail states and/or reducing the effective doping, thereby increasing ρ. Subsequent LiSo may partially reverse these changes by enabling hydrogen-assisted rebonding and partial recovery of the electronic structure, leading to the observed reduction in ρ. At the same time, a residual resistivity offset may reflect a microstructural modification that is not fully annealed under the moderate LiSo temperature.

To test the hypothesis, additional microstructural characterization was performed. Figure 6a shows the grazing incidence X-ray diffraction (GI-XRD) patterns of TPC samples before and after UV exposure to a UV dose of 15 kWh m^{-2}, normalized for comparison. Both patterns display diffraction peaks consistent with 3C-SiC (111), (220), and (311) [37]. A broad feature at approximately $2\vartheta = 56.1°$ could originate from the c-Si substrate, consistent with its (311) diffraction peak. The broad peaks between $2\vartheta = 30°$–$40°$ were deconvoluted using two Voigt functions, as shown in Figure 6b,c. The dominant peak at $2\vartheta = 35.5°$ is assigned to the 3C-SiC (111) diffraction peak, while the shoulder at around $2\vartheta = 33.8°$ is commonly attributed to stacking faults in the cubic SiC lattice [38]. Comparing the two GI-XRD patterns, the 3C-SiC (111) intensity increases markedly after UV exposure, whereas the (220) peak remains essentially unchanged and the (311) peak is barely discernible. This implies an increased crystallinity and enhanced orientation preference due to UV exposure. Owing to the limited number o$D = \frac{K\lambda}{\beta\cos\vartheta}$f well-resolved peaks (primarily (111) and (220)), a conventional Williamson–Hall analysis to distinguish the grain size and microstrain effects in the SiC layer cannot be applied [39]. Instead, simple analysis based on the Scherrer equation (Equation (3)) and residual stress equation (Equation (4)) is applied to estimate the mean coherent diffraction domain size (D) and residual stress (σ) in both samples.

$$D = \frac{K\lambda}{\beta\cos\vartheta} \tag{3}$$

$$\sigma = \frac{E}{1+\nu} \cdot \frac{d - d_0}{d_0} \tag{4}$$

In the Scherrer equation, β is the full width at half maximum (FWHM) of the 3C-SiC (111) peak, K is the dimensionless shape factor (0–1), where K is 0.9 [38], and ϑ is the Bragg angle. In Equation (4), σ is the residual stress with unit of GPa, E is the Young's modulus using the value (450.19 GPa) in ref. [38], ν is Poisson's ratio ($\nu = 0.19$) [40], and d and d_0 are the interplanar spacings calculated from the peak position in the GI-XRD pattern and using the standard 3C-SiC (111) peak with $2\vartheta = 36.2°$ by Bragg equation.

After UV irradiation to 15 kWh m^{-2}, D of the nc-SiC:H layer decreases from 4.51 to 3.57 nm, while the residual stress increases from 1.72 to 1.94 GPa. The reduction in D can be reconciled with the increased GI-XRD intensity if UV exposure promotes a local amorphous-to-nanocrystalline transformation, yielding a larger crystalline fraction but smaller coherent domains and/or enhanced microstrain. This interpretation appears most plausible in view of the microstructural picture suggested above for the nc-SiC:H stack, particularly the passivation layer, where the amorphous phase is distributed between nano crystallites. The initial residual stress already exceeds that of a monocrystalline system [41], suggesting that the nc-SiC:H layer is in a metastable, non-equilibrium state and may readily undergo local structural transformations. Newly crystallized regions formed under the low-temperature UV condition are likely to be defect-rich (e.g., containing stacking faults and unsaturated bonds), which can increase electronic disorder by introducing additional localized states such as band-tail or defect states and may reduce the effective doping in the nc-SiC:H stack.

To obtain spatially resolved structural evidence following the GI-XRD analysis, four-dimensional scanning transmission electron microscopy (4D-STEM) was performed on specimens prepared from TPC solar cells. 4D-STEM enables orientation- and phase-mapping with high spatial resolution, allowing the nc-SiC:H layers to be quantified in terms of local crystallinity [42]. Measurements were performed by first aligning the sample to a low-index zone axis of the c-Si substrate, followed by recording a diffraction pattern at each probe position. Orientation maps were

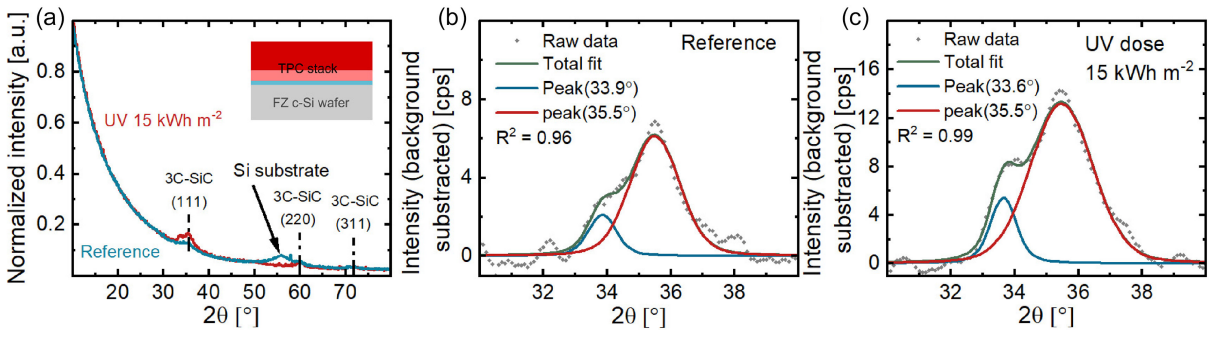

FIGURE 6 | (a) Grazing-angle incidence X-ray diffraction patterns of TPC samples before and after 15 kWh m^{-2} UV exposure. The samples comprise a double-layer nc-SiC:H stack deposited on Piranha-oxidized, polished c-Si wafers. Deconvoluted 3C-SiC (111) broad peak for TPC samples (b) before and (c) after UV exposure.

then reconstructed by indexing the diffraction patterns using a template-matching (diffraction-matching) algorithm.

Figure 7a,b shows virtual bright-field (BF) images of the entire front-side cross section of the TPC specimens before and after UV irradiation at a dose of 30 kWh m^{-2}. Columnar-grown ITO grains are uniformly distributed in both specimens, with no discernible UV-induced change, consistent with the analysis in Figure 4. Zoomed-in BF images of TPC contact region are shown in Figure 7c,d. In both cases, crystal contrast from SiC nanocrystals is visible. Notably, a larger bright-contrast region appears at the TPC/c-Si interface before UV exposure, which may indicate a locally porous or low-density phase. To further probe possible structural changes in this region, near-real-time orientation mapping and phase-reliability analysis were performed. The resulting orientation maps were displayed using an inverse pole figure (IPF) color code. Figure 7m provides the IPF keys for cubic c-Si/3C-SiC and hexagonal ITO. Phase-reliability maps are shown in Figure 7e,f, and the corresponding z-direction orientation maps are shown in Figure 7g,h. Because a 3C-SiC template was used for matching, blank regions in the phase-reliability and orientation maps indicate areas that cannot be indexed as 3C-SiC, consistent with an amorphous fraction within the nc-SiC:H stack. Figure 7i–l shows representative experimental diffraction patterns from the regions marked in Figure 7c,d. The diffraction pattern exhibits a combination of sharp diffraction spots arranged in concentric rings and diffuse halos. This mixed feature suggests a structure in which the nanocrystalline phases are embedded in an amorphous matrix. High-magnification BF and annular dark-field (ADF) STEM images of the TPC/c-Si interfaces were acquired using a probe spherical-aberration-corrected system. The corresponding fast Fourier transform (FFT) images, extracted from selected BF regions, corroborate the template-matching results, as shown in Figure S15. By comparing the phase-reliability and orientation maps of the specimens before and after UV exposure, a reduced amorphous fraction is observed in the nc-SiC:H stack after UV irradiation, consistent with localized crystallization. These observations are consistent with the hypothesis of a local microstructural transformation proposed above and

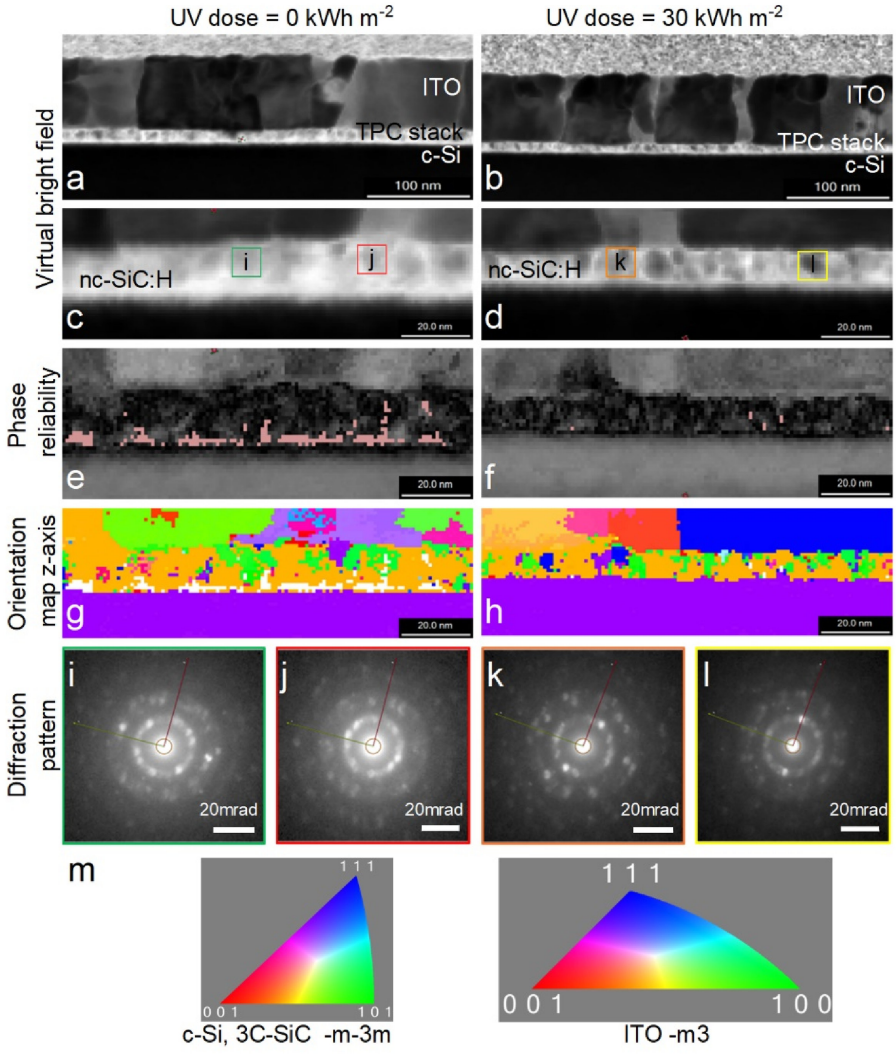

FIGURE 7 | Scanning transmission electron microscopy (STEM) images of TPC specimens from solar cells before and after UV exposure at a dose of 30 kWh m^{-2}: (a,b) virtual bright-field images of the entire front side, (c,d) magnified regions of the TPC stack, (e,f) phase reliability maps, (g,h) grain orientation maps, and (i–l) experimental diffraction patterns for selected areas (indicated by the frames in c,d). (m) Inverse pole figures for the c-Si substrate, 3C-SiC, and ITO layers.

provide complementary insights into the structural interpretation derived from the GI-XRD results. However, the microscopic driving mechanism, particularly how H-related processes trigger the structural changes, remains to be elucidated and warrants further investigation.

3 | Conclusion

This study demonstrates that the severity of UVID in silicon heterojunction solar cells is strongly governed by the illuminated-side passivating-contact design. Compared with conventional a-Si:H-based SHJ contacts, nc-SiC:H-based TPC contacts enables much stronger losses in V_{OC}, J_{SC}, and FF under an identical UV irradiation, where the FF reduction is dominated by an increase in R_s. The results support a unified picture in which the high optical transparency of TPC shifts the UV energy deposition through thermalization toward the c-Si near-interface region, thereby promoting Si—H bond rupture and the formation of recombination centers that degrade the chemical passivation and the spectral response. In parallel, UV exposure induces a pronounced resistivity increase in the nc-SiC:H stack, consistent with local microstructural rearrangements and enhanced electronic disorder, with sub-bandgap absorption as a plausible contributing factor. FTIR shows UV-induced changes in Si-H bonding, while SIMS excludes pronounced long-range hydrogen redistribution across interfaces within its depth resolution. LiSo largely restores the lifetime and resistivity, yet leaves a residual, non-fully recoverable component under the applied protocol. GI-XRD and STEM provide complementary evidence for a UV-induced localized crystallization.

Conclusively, these findings highlight that highly transparent front contacts require explicit UV management. Future TPC optimization should minimize sub-bandgap absorption and defect-rich structural evolution in nc-SiC:H, while module-level UV-blocking or UV-downshifting encapsulation offers a practical route to mitigate UVID and improve long-term stability.

4 | Experimental Details

Czochralski (CZ) grown n-type c-Si wafers (1 Ω cm, <100>, LONGi) were used for solar cells and symmetric samples. After saw-damage removal and standard texturing, 157.35 mm × 157.35 mm wafers were quartered, ozone cleaned and dipped in 1% hydrofluoric acid (HF) for 5 min prior to deposition. For TPC samples, a wet-chemical Piranha oxidation was applied to form a SiO_X tunneling layer (process details in Ref. [17]). Conventional SHJ front contacts (a-Si:H(n)/a-Si:H(i)) and rear contacts (a-Si:H(i)/a-Si:H(p)) were deposited at 200°C in a Meyer Burger AK1000 Plasma-enhanced chemical vapor deposition (PECVD) system using hydrogen (H_2) and silane (SiH_4) with phosphine (PH_3) and diborane (B_2H_6) as dopants. TPC front contact based on n-type nc-SiC:H were deposited by MRG Hot-wire chemical vapor deposition (HWCVD) system at a chamber temperature of 250°C using H_2, 5% monomethylsilane (MMS) diluted in H_2, and nitrogen (N_2) as precursor gases. The double-layer stack comprised a passivation layer deposited at filament temperature (T_f) = 1700°C for 4 min and a conductive layer at T_f = 2000°C for 30 min. Sn-doped indium oxide (ITO) layer was sputtered from a rotational 3 wt% doped ITO target at 150°C in a Von Ardenne VISS 300 system. Front ITO was deposited at 1 kW and 3.6 μbar, and rear ITO was deposited at 4 kW and 3.5 μbar. For solar cells, customized masks were applied during sputtering to define a 2 cm × 2 cm active area. Metallization was performed by screen-printing Ag paste (NAMICS) using a Microtec MT-650TVC screen printer, followed by drying at 150°C for 10 min and curing at 170°C for 40 min. Prior to UV exposure, samples were pre-treated by LiSo in in a GSOLA GLR-4Z system. Fabrication sequences for solar cells and symmetric samples, and LiSo details can be found in our recent paper [35, 36].

The injection-dependent effective lifetime was measured by transient photoconductance decay (Sinton WCT-120). Current-voltage characteristics, spectral response (EQE) and device reflectance were measured using a pv-tools LOANA system equipped with a Wavelabs Sinus 220 LED light source. Contact resistivity (ρ_c) was extracted by transfer length method (TLM) with customized patterns fabricated on the same solar-cell wafer in an in-house setup. Corning EAGLE XG glass served as the substrate for transmittance and reflectance (T&R) and Hall measurement samples. The T&R measurements were performed using a Perkin Elmer Lambda 950 UV–vis spectrophotometer. Hall measurements were done by the van der Pauw method at room temperature to extract resistivities (ρ). FTIR was used to analyze the evolution of the chemical composition of nc-SiC:H, where the float-zone (FZ) grown, double-side polished silicon wafer (20 mm × 20 mm) served as the substrate. SIMS was performed using two instruments. Elemental depth profiles in Figures 5 and S10 were acquired on an IONTOF ToFSIMS5.ncs instrument using 1 kV Cs^+ ions for sputtering (300 × 300 μm^2) and 30 kV Bi^+ ions for analysis (40 × 40 μm^2). The contact stack was deposited on a Piranha-oxidized float-zone (FZ) wafer as a sample. Quantified H concentration profiles in Figure S11 were measured on a CAMECA IMS-7f Auto Mangetic Sector SIMS using 1.5 kV O_2^+ ions for analysis (diameter ϕ = 60 μm). GI-XRD was conducted in a Bruker D8 advance (2ϑ = 10°–80°, incident angle ω = 0.4°) in a parallel beam setup (Goebel mirror) and using a primary beam aperture of 0.6 mm and a secondary equatorial Soller slit (0.3°). A fully opened LYNXEYE-XE 1D detector was used to enhance the signal-to-noise ratio.

4D-STEM analysis was performed on a TESCAN TENSOR operated at 100 kV with integrated near-real-time data acquisition and processing. Cross-sectional lamellae were prepared by focused ion beam (FIB). Diffraction patterns were recorded along the [110] direction of the c-Si substrate. The experiment was conducted with 2 nm pixel size and 2 mrad convergence semi-angle, generating a probe size of approximately 1.169 nm and probe current of 266.7 pA. The scanning area was 300 nm × 300 nm, providing a resolution of approximately 1.69 nm per probe size. More details of the 4D-STEM characterization can be found in another work [42]. Atomic-resolution STEM images (Figure S15) were acquired on an aberration-corrected JEOL ARM300F2 operated at 300 kV. The convergence semi-angle was set to 24.9 mrad, with ADF and BF signals were collected over 45–180 and 0–30 mrad, respectively. Image processing was performed using DigitalMicrograph (Gatan).

Author Contributions

Binbin Xu: conceptualization (equal), data curation (lead), formal analysis (equal), investigation (lead), methodology (equal), resources (equal), validation (lead), visualization (lead), writing – original draft (lead); writing – review and editing (lead). **Sara Alkhereibi:** data curation (equal), formal analysis (equal), investigation (equal), methodology (equal), resources (equal), software (lead), validation (equal), visualization (equal), writing – review and editing (equal). **Alexander Eberst:** conceptualization (supporting), formal analysis (supporting), investigation (supporting), methodology (supporting), project administration (lead), resources (supporting), writing – review and editing (equal). **Kai Zhang:** conceptualization (equal), investigation (supporting), methodology (supporting), visualization (supporting), writing – review and editing (equal). **Rongda Zhang:** conceptualization (supporting), formal analysis (supporting), investigation (supporting), methodology (supporting), validation (supporting), writing – review and editing (supporting). **Joon-Ho Oh:** methodology (supporting), resources (equal), visualization (supporting), writing – review and editing (equal). **Astrid Besmehn:** investigation (equal), resources (equal), writing – review & editing (supporting). **Felix Gunkel:** investigation (equal), resources (equal). **Yuehui Li:** investigation (equal), resources (equal), writing – review and editing (supporting). **Tae Eun Hong:** investigation (equal), resources (equal). **Andreas Lambertz:** conceptualization (supporting), funding acquisition (equal), methodology (supporting), project administration (equal), resources (equal). **Karsten Bittkau:** conceptualization (equal), formal analysis (equal), methodology (equal), project administration (supporting), visualization (equal), writing – review and editing (equal). **Joachim Mayer:** supervision (equal). **Uwe Rau:** conceptualization (supporting), formal analysis (supporting), funding acquisition (supporting), methodology (supporting), supervision (lead). **Kaining Ding:** conceptualization (equal), funding acquisition (lead), project administration (equal), resources (equal), supervision (equal), writing – review and editing (supporting).

Acknowledgments

We gratefully thank T. Birrenbach and N. Bongartz for regular checks and spectral measurements of the UV chamber. We thank J. Wolff and A. Schmalen for the daily maintenance of the HWCVD system. We thank the support from the B. Zwaygardt, A. Doumit, H. Siekmann, V. Lauterbach, A. Mück, and S. Lynen for laser cutting, cleaning and texturing of wafers, depositions of a-Si:H and ITO layer, metallization, and light soaking treatment. This work was supported by the Helmholtz Nano Facility funded by the Helmholtz Association [43]. We are grateful to the Spherical Aberration Corrected Transmission Electron Microscopy Center, Henan Academy of Sciences for their support in the preparation of TEM samples and the acquisition of high-resolution STEM images for Figure S15. JHO gratefully acknowledges the financial support provided by the Global Joint Research Promotion Program, jointly managed by Forschungszentrum Jülich and the National Research Council of Science and Technology (NST) of the Ministry of Science and ICT (MSIT) of Korea (grant no. NST-Global-24-001). B.X. thanks the financial support by the China Scholarship Council (CSC, No. 202106830034).

Open Access funding enabled and organized by Projekt DEAL.

Funding

This study was supported by the China Scholarship Council (202106830034) and the Ministry of Science and ICT, South Korea (NST-Global-24-001).

Conflicts of Interest

The authors declare no conflicts of interest.

Data Availability Statement

The data that support the findings of this study are available from the corresponding author upon reasonable request.

Resource Availability

Lead Contact: Further information and requests for resources should be directed to and will be fulfilled by lead contact, Alexander Eberst (a.eberst@fz-juelich.de).

Materials Availability

This study did not generate new unique materials.

Data and Code Availability

The raw data and data supporting this study are available from the lead contact upon reasonable request. This study does not report any original codes or algorithms.

References

1. H. Wu, F. Ye, M. Yang, et al., "Silicon Heterojunction Back-Contact Solar Cells by Laser Patterning," *Nature* 635 (2024): 604–609, https://doi.org/10.1038/s41586-024-08110-8.

2. E. Aydin, T. G. Allen, M. De Bastiani, et al., "Pathways toward Commercial Perovskite/Silicon Tandem Photovoltaics," *Science* 383 (2024): eadh3849, https://doi.org/10.1126/science.adh3849.

3. H. Zhang, L. Zhang, W. Liu, et al., "Influence of Intrinsic Amorphous Silicon Passivation Layer on the Dark-State Stability of SHJ Cells," *Applied Physics Letters* 122 (2023): 182101, https://doi.org/10.1063/5.0144574.

4. O. A. Arruti, A. Virtuani, and C. Ballif, "Long-Term Performance and Reliability of Silicon Heterojunction Solar Modules," *Progress in Photovoltaics: Research and Applications* 31 (2023): 664–677, https://doi.org/10.1002/pip.3688.

5. W. Liu, L. Zhang, X. Yang, et al., "Damp-Heat-Stable, High-Efficiency, Industrial-Size Silicon Heterojunction Solar Cells," *Joule* 4 (2020): 913–927, https://doi.org/10.1016/j.joule.2020.03.003.

6. O. A. Arruti, L. Gnocchi, Q. Jeangros, C. Ballif, and A. Virtuani, "Potential-Induced Degradation in Bifacial Silicon Heterojunction Solar Modules: Insights and Mitigation Strategies," *Progress in Photovoltaics: Research and Applications* 32 (2024): 304–316, https://doi.org/10.1002/pip.3765.

7. A. Sinha, J. Qian, S. L. Moffitt, et al., "UV-Induced Degradation of High-Efficiency Silicon PV Modules with Different Cell Architectures," *Progress in Photovoltaics: Research and Applications* 31 (2023): 36–51, https://doi.org/10.1002/pip.3606.

8. H. Ye, S. Huang, C. Qian, et al., "Short Wavelength Photons Destroying Si−H Bonds and Its Influence on High-Efficiency Silicon Solar Cells and Modules," *Solar RRL* 7 (2023): 2300334, https://doi.org/10.1002/solr.202300334.

9. L. Yang, Z. C. Hu, Q. Y. He, et al., "Insights into Mechanism of UV-Induced Degradation in Silicon Heterojunction *Solar Cells*," *Solar Energy Materials and Solar Cells* 275 (2024): 113022, https://doi.org/10.1016/j.solmat.2024.113022.

10. J. L. Yang, Y. H. Tang, C. L. Zhou, et al., "Unveiling the Mechanism of Ultraviolet-Induced Degradation in Silicon Heterojunction *Solar Cells*," *Solar Energy Materials and Solar Cells* 276 (2024): 113062, https://doi.org/10.1016/j.solmat.2024.113062.

11. B. Xu, K. Bittkau, A. Eberst, et al., "Downshifting Encapsulant: Optical Simulation Evaluation of the Solution to Ultraviolet-Induced Degradation in Silicon Heterojunction Solar Cells," *Advanced Energy and Sustainability Research* 6 (2025): 2400227, https://doi.org/10.1002/aesr.202400227.

12. F. T. Thome, P. Meßmer, S. Mack, et al., "UV-Induced Degradation of Industrial PERC, TOPCon, and HJT Solar Cells: The Next Big Reliability Challenge?," *Solar RRL* 8 (2024): 2400628, https://doi.org/10.1002/solr.202400628.

13. Q. Yang, K. Bittkau, A. Eberst, U. Rau, and K. Ding, "The Impact of Interface Recombination on the External Quantum Efficiency of Silicon Solar Cells," *Solar Energy Materials and Solar Cells* 273 (2024): 112953, https://doi.org/10.1016/j.solmat.2024.112953.

14. M. Köhler, M. Pomaska, P. Procel, et al., "A Silicon Carbide-Based Highly Transparent Passivating Contact for Crystalline Silicon Solar Cells Approaching Efficiencies of 24%," *Nature Energy* 6 (2021): 529–537, https://doi.org/10.1038/s41560-021-00806-9.

15. F. E. Rougieux, C. Sen, M. Abbott, and B. Hoex, "Light-Activated Surface Passivation for More Efficient Silicon Heterojunction Solar Cells: Origin, Physics and Stability," *Solar Energy Materials and Solar Cells* 269 (2024): 112789, https://doi.org/10.1016/j.solmat.2024.112789.

16. S. De Wolf and M. Kondo, "Nature of Doped *a*-Si: H/c-Si Interface Recombination," *Journal of Applied Physics* 105 (2009): 103707, https://doi.org/10.1063/1.3129578.

17. M. Köhler, M. Pomaska, F. Lentz, F. Finger, U. Rau, and K. Ding, "Wet-Chemical Preparation of Silicon Tunnel Oxides for Transparent Passivated Contacts in Crystalline Silicon Solar Cells," *ACS Applied Materials & Interfaces* 10 (2018): 14259–14263, https://doi.org/10.1021/acsami.8b02002.

18. K. T. Regner, D. P. Sellan, Z. Su, C. H. Amon, A. J. H. McGaughey, and J. A. Malen, "Broadband Phonon Mean Free Path Contributions to Thermal Conductivity Measured Using Frequency Domain Thermoreflectance," *Nature Communications* 4 (2013): 1640, https://doi.org/10.1038/ncomms2630.

19. C. G. Van de Walle, "Energies of Various Configurations of Hydrogen in Silicon," *Physical Review B* 49 (1994): 4579–4585, https://doi.org/10.1103/PhysRevB.49.4579.

20. Y. Pan, J. Zhou, and G. Chen, "Quantifying Thermal Transport in Amorphous Silicon Using Mean Free Path Spectroscopy," *Physical Review B* 101 (2020): 144203, https://doi.org/10.1103/PhysRevB.101.144203.

21. K. Bushick and E. Kioupakis, "Phonon-Assisted Auger-Meitner Recombination in Silicon from First Principles," *Physical Review Letters* 131 (2023): 076902, https://doi.org/10.1103/PhysRevLett.131.076902.

22. D. L. Staebler and C. R. Wronski, "Reversible Conductivity Changes in Discharge-Produced Amorphous Si," *Applied Physics Letters* 31 (1977): 292–294, https://doi.org/10.1063/1.89674.

23. M. Stutzmann, W. B. Jackson, and C. C. Tsai, "Light-Induced Metastable Defects in Hydrogenated Amorphous Silicon: A Systematic Study," *Physical Review B* 32 (1985): 23–47, https://doi.org/10.1103/physrevb.32.23.

24. M. Cowie, P. C. Constantinou, N. J. Curson, T. J. Z. Stock, and P. Grutter, "Spatially Resolved Random Telegraph Fluctuations of a Single Trap at the Si/SiO(2) Interface," *Proceedings of the National Academy of Sciences* 121 (2024): e2404456121, https://doi.org/10.1073/pnas.2404456121.

25. S. Olibet, E. Vallat-Sauvain, and C. Ballif, "Model for a-Si: H/c-Si Interface Recombination Based on the Amphoteric Nature of Silicon Dangling Bonds," *Physical Review B* 76 (2007): 035326, https://doi.org/10.1103/PhysRevB.76.035326.

26. Y. Yamashita, A. Asano, Y. Nishioka, and H. Kobayashi, "Dependence of Interface States in the Si Band Gap on Oxide Atomic Density and Interfacial Roughness," *Physical Review B* 59 (1999): 15872–15881, https://doi.org/10.1103/PhysRevB.59.15872.

27. T. F. Schulze, H. N. Beushausen, C. Leendertz, A. Dobrich, B. Rech, and L. Korte, "Interplay of Amorphous Silicon Disorder and Hydrogen Content with Interface Defects in Amorphous/Crystalline Silicon Heterojunctions," *Applied Physics Letters* 96 (2010): 252102, https://doi.org/10.1063/1.3455900.

28. B. R. Tuttle, "Dangling Bond Defects in SiC: An Ab Initio Study," *Physical Review B* 97 (2018): 045203, https://doi.org/10.1103/PhysRevB.97.045203.

29. I. Hamberg and C. G. Granqvist, "Evaporated Sn-Doped In2O3 Films: Basic Optical Properties and Applications to Energy-Efficient Windows," *Journal of Applied Physics* 60 (1986): R123–R160, https://doi.org/10.1063/1.337534.

30. B. Fischer, A. Lambertz, M. Nuys, et al., "Insights into the Si - H Bonding Configuration at the Amorphous/Crystalline Silicon Interface of Silicon Heterojunction Solar Cells by Raman and FTIR Spectroscopy," *Advanced Materials* 35 (2023): e2306351, https://doi.org/10.1002/adma.202306351.

31. M. Katiyar, Y. H. Yang, and J. R. Abelson, "Si−C−H Bonding in Amorphous Si1−xCx: H Film/Substrate Interfaces Determined by Real Time Infrared Absorption during Reactive Magnetron Sputter Deposition," *Journal of Applied Physics* 78 (1995): 1659–1663, https://doi.org/10.1063/1.360260.

32. G. V. Soares, I. J. R. Baumvol, C. Radtke, and F. C. Stedile, "Enhanced Hydrogen Bonding Strength Observed in Hydrogenated SiC and SiO_2/SiC Structures," *Applied Physics Letters* 90 (2007): 081906, https://doi.org/10.1063/1.2645341.

33. A. Eberst, A. Lambertz, W. Duan, V. Smirnov, U. Rau, and K. Ding, "Material Properties of Nanocrystalline Silicon Carbide for Transparent Passivating Contact Solar Cells," *Solar RRL* 7 (2023): 2300013, https://doi.org/10.1002/solr.202300013.

34. W. Beyer, M. Nuys, G. Andrä, et al., "Secondary Ion Mass Spectrometry Study of Hydrogenated Amorphous Silicon Layer Disintegration upon Rapid (Laser) Annealing," *Physica Status Solidi (a)* 220 (2023): 2200671, https://doi.org/10.1002/pssa.202200671.

35. B. Xu, A. Eberst, P. Fall, et al., "Restoring Sputter Damage by Light Soaking in Silicon Carbide-Based Transparent Passivating Contact Solar Cells," *Cell Reports Physical Science* 6 (2025): 102552, https://doi.org/10.1016/j.xcrp.2025.102552.

36. W. Duan, T. Rudolph, H. T. Gebrewold, et al., "Insights into the Heat-Assisted Intensive Light-Soaking Effect on Silicon Hetero-junction Solar Cells," *Solar RRL* 8 (2024): 2400383, https://doi.org/10.1002/solr.202400383.

37. L. Zhang, W. Jiang, W. Ai, L. Chen, C. Pan, and T. Wang, "Grain Size Variation in Nanocrystalline Silicon Carbide Irradiated at Elevated Temperatures," *Journal of the American Ceramic Society* 102 (2019): 448–455, https://doi.org/10.1111/jace.15895.

38. V. V. Pujar and J. D. Cawley, "Effect of Stacking Faults on the X-Ray Diffraction Profiles of β-SiC Powders," *Journal of the American Ceramic Society* 78 (1995): 774–782, https://doi.org/10.1111/j.1151-2916.1995.tb08246.x.

39. N. M. Sultan, T. M. B. Albarody, H. K. M. Al-Jothery, M. A. Abdullah, H. G. Mohammed, and K. O. Obodo, "Thermal Expansion of 3C-SiC Obtained from In-Situ X-Ray Diffraction at High Temperature and First-Principal Calculations," *Materials* 15 (2022): 6229.

40. W. L. Zhu, J. L. Zhu, S. Nishino, and G. Pezzotti, "Spatially Resolved Raman Spectroscopy Evaluation of Residual Stresses in 3C-SiC Layer Deposited on Si Substrates with Different Crystallographic Orientations," *Applied Surface Science* 252 (2006): 2346–2354, https://doi.org/10.1016/j.apsusc.2005.04.020.

41. S. Sapienza, M. Ferri, L. Belsito, et al., "Measurement of Residual Stress and Young's Modulus on Micromachined Monocrystalline 3C-SiC Layers Grown on <111> and <100> Silicon," *Micromachines* 12 (2021): 1072.

42. S. Alkhereibi, M. A. Yaqin, A. Eberst, et al., "Resolving the Microstructure of Aluminum-Doped Zinc Oxide Thin Films Grown

on Different Silicon Heterojunction Solar Cell Structures by Advanced Transmission Electron Microscopy," *Thin Solid Films* 825 (2025): 140744, https://doi.org/10.1016/j.tsf.2025.140744.

43. W. Albrecht, J. Moers, and B. Hermanns, "HNF - Helmholtz Nano Facility," *Journal of Large-Scale Research Facilities JLSRF* 3 (2017): A112, https://doi.org/10.17815/jlsrf-3-158.

Supporting Information

Additional supporting information can be found online in the Supporting Information section.